Catalysis Today 168 (2011) 124–132

Contents lists available at ScienceDirect

Catalysis Today

journal homepage: www.elsevier.com/locate/cattod

The hierarchical effects of zeolite composites in catalysis

Jiajun Zheng[a], Qinghu Zeng[a], Yuming Yi[a], Yan Wang[a], Jinghong Ma[a], Bo Qin[b], Xiwen Zhang[b], Wanfu Sun[b], Ruifeng Li[a,*]

[a] Key Laboratory of Coal Science and Technology MOE, Institute of Special Chemicals, Taiyuan University of Technology, Taiyuan 030024, China
[b] Fushun Research Institute of Petroleum and Petrochemicals, SINOPEC, Fushun 113001, China

ARTICLE INFO

Article history:
Received 30 September 2010
Received in revised form 6 January 2011
Accepted 10 January 2011
Available online 4 February 2011

Keywords:
Zeolite composite
Hierarchical pores
Tunable acidity
Diffusion
Hierarchy factor (HF)

ABSTRACT

A series of zeolite composites with hierarchically porous structures and tunable acidities were prepared. The structural, crystalline, and textural properties of the as-synthesized materials, as well as the reference Y and β zeolite samples, were characterized by X-ray diffraction (XRD), scanning electron microscopy (SEM)/transmission electron microscopy (TEM) analyses, Fourier transform infrared spectroscopy (FTIR), and nitrogen adsorption/desorption techniques. The acidic properties of the surface were determined by in situ FTIR of adsorbed pyridine. The hierarchy factor is an appropriate tool to classify hierarchically structured materials, and the hierarchical pores of the as-synthesized zeolite composite samples were investigated during the catalytic cracking of isopropylbenzene. The results show that the catalytic activity of isopropylbenzene cracking over the catalysts has a linear dependence with their hierarchy factor (HF). The tunable acidities were tested by methanol dehydration to dimethyl ether (DME), and the dehydration activity of methanol over the catalysts shows a linear decrease with the increased Lewis/Brönsted ratio, while the selectivity of DME shows a linear increase with the enhanced Lewis/Brönsted ratio.

1. Introduction

Due to the similarity between the size of the involved guest molecules and the micropore diameter, zeolites, which are widely used in heterogeneous catalysis as well as in separation and purification fields, have been hampered by their small microporous channels. These channels are subject to diffusion limitations on reaction rates because they restrict the transport of molecules to and from the active sites located within the micropores [1–4]. Intracrystalline diffusion inside a zeolite micropore at a given temperature and pressure cannot be increased without changing the internal pore architecture, which limits the effective utilization of acidic sites by bulky molecules. In hydrocarbon transformation over zeolites, the conversion depends on both the probability of the reactants accessing the acidic sites and the time the reactant molecules spend inside zeolite crystals [5]. As a consequence, improving the transport of molecules in microporous crystals is attracting significant research interest [5–7]. For a given zeolite material, the basic strategy to improve diffusion is to shorten the length of the micropore channels [2,3,6–13] or to widen the pore diameter. In zeolites, this can be accomplished by decreasing the crystal size or by introducing an additional (meso) pore system within an individual zeolite crystal [2].

In the past decades, a considerable number of attempts have been devoted to minimizing the diffusion limitation of micropores in zeolites by adjusting their crystal sizes to nanoscale ranges, which has been achieved by adding growth inhibitors, by increasing supersaturation, or by quenched crystallization [2]. However, none of these attempts produced an easy means of controlling the crystal size [14]; the colloidal properties makes separating the small zeolite crystals from the reaction mixture a difficult task [2], and this severely hinders their practical applications. Moreover, the volume and surface area of the micropores in the nano-sized zeolites were lower because the ordering of the three-dimensional network of the zeolite particles deteriorated [15]. Another approach to improve diffusion in the given zeolite materials is to insert meso- or macropores into zeolite particles [6,7,15–19]. Because the diffusion in mesopores is several orders of magnitude faster than that in micropores, the created meso- or macroporosity facilitates physical transport and leads to a more effective use of these materials [6,7,20]. In this way, the micropores of the zeolite have been effectively shortened, and their molecular accessibility has been largely enhanced [5,21,22]. The hierarchical pores in the micropore zeolite crystal can be created by a post-treatment [6–13,19,23] or templated approach [15,24–29]. The introduction of mesopores in the micropore zeolite by post-treatment has been mainly concentrated on alkali-leaching [6–9] and acid-leaching [1] as well as

---

* Corresponding author at: Institute of Special Chemicals, Taiyuan University of Technology, 79# West Yingze Street, Taiyuan 030024, China. Fax: +86 351 6010121.
E-mail addresses: rfli@tyut.edu.cn, ruifeng_li@hotmail.com (R. Li).

0920-5861/$ – see front matter © 2011 Elsevier B.V. All rights reserved.
doi:10.1016/j.cattod.2011.01.006

steaming. In recent years, using a template to synthesize hierarchical pores zeolites has been shown to be very effective. Jacobsen et al. [25,26] synthesized mesoporous zeolite crystals using a carbon matrix with a mesopore system or multiwall carbon nanotubes as the mesopore-forming agents. Tao et al. [15,27–29] reported a method of preparing meso-zeolite with a carbon aerogel with uniform mesopores as the template. The zeolite crystals were nucleated within the three-dimensional mesoporous system of carbon aerogels. Removal of the carbon aerogels by burning resulted in a monolithic zeolite with a mesoporous system.

Despite the fact that hierarchal materials have been extensively researched, however, the question of whether the quantity of the mesopores introduced into microporous materials is appropriate and optimal had not been reported until Pérez-Ramírez studied the effect of alkalinity on the mesopore formation in the ZSM-5 zeolite [30]. The preparation of hierarchal materials should pursue a strategy that encompasses forming extensive mesoporosity while minimizing the loss in microporosity. Pérez-Ramírez et al. [30] thought that the excessive introduction of meso- or/and macropores into zeolites was not beneficial, as the penalty paid in the micropore volume rendered a less efficient catalyst. They therefore put forward a conception of the HF (hierarchy factor) and showed that it is an appropriate tool to classify hierarchically structured materials. The latter point is of interest to the scientific community as it not only embraced mesoporous zeolites obtained by desilication methods but also enabled a quantitative comparison and correlation of various materials obtained by different synthetic methodologies [30].

In this paper, we synthesize a series of zeolite composites by employing a β or Y zeolite as the nutrient for the other phase of zeolite growth. We selected the catalytic cracking of isopropylbenzene and the dehydration of methanol to DME to investigate the performance effects of the hierarchical pores and the tunable acidity, respectively, in the as-synthesized zeolite composite catalysts. The relationships between the catalytic activity and the hierarchy factor (HF) or Lewis/Brönsted ratio (L/B ratio) of the different catalysts with different porosities and related acidities were investigated.

2. Experimental

2.1. Synthesis

BFZ (a composite zeolite prepared using β zeolite as the core and Y zeolite as the shell): β zeolite was prepared with the following molar composition: $2.2Na_2O:20SiO_2:Al_2O_3:4.6(TEA)_2O:4.6(NH_4)_2O:440H_2O$. It was then hydrothermally treated at 413 K for 240 h. A volume of 72 mL of the reacted mixture that contained the pre-synthesized β zeolite was directly used in the second step of the synthesis. Then 3.0 g sodium aluminate and 3 mL seeds of Y zeolite were added to the reacted mixture, and the value of $[OH^-]$ in the synthesis solution was adjusted to 1.0–2.0 mol/L by adding sodium hydroxide or concentrated sulfuric acid. The solution was then stirred for 2 h at room temperature. The new mixture was then loaded into an autoclave for hydrothermal treatment at 363 K for 18 h under autogenous pressure. The as-synthesized solid product was recovered by filtration, washed with water, dried in air at 373 K overnight, and denoted as BFZ-*x* (*x* stands for the concentration of OH^- in units of mol/L).

BFZ-s (a composite zeolite prepared with β zeolite-embedded aluminosilicate extrudates as the nutrients for Y zeolite growth): The fabrication of BFZ-*s* (shaped) zeolite composites generally involved preparation of the β zeolite-embedded aluminosilicate extrudates followed by the hydrothermal transformation process. The β zeolite-containing aluminosilicate extrudates were typically prepared as follows: 100 g of β zeolite powder ($SiO_2/Al_2O_3 = 25$), 80 g of $NaAlO_2$, 150 mL of silica sol and 60 mL of Y zeolite seeds were well mixed with an appropriate amount of pseudoboehmite or/and amorphous silica-alumina as the binders [31]. The mixtures were then kneaded and extruded into cylindrically shaped extrudates with a diameter of ~2.0 mm. After drying at 373 K, 8 g of the extrudates, 2 mL of Y zeolite seeds, and 2 g of sodium hydroxide were added to 72 mL water and put in a stainless steel autoclave. The autoclaves were then enclosed and heated at 363 K. After crystallization for 12 h, the as-synthesized solid product was recovered by filtration, washed with water, dried in air at 373 K overnight and denoted as BFZ-*s*.

FBZ (a composite zeolite prepared with Y zeolite as the core as well as the nutrients for β zeolite growth) was prepared using the procedure proposed in one of our recent studies [31].

FAU-BEA (a composite zeolite obtained by the overgrowth of β zeolite on the core Y crystal) was prepared using the procedure proposed in another of our recent studies [32].

Pure phase zeolite Y ($SiO_2/Al_2O_3 = 5$) and zeolite β ($SiO_2/Al_2O_3 = 25$) were used as references. All the as-synthesized samples were calcined in air at 823 K for 5 h, and the NH_4^+ form of the sample was obtained by performing an ion exchange with 0.5 M NH_4NO_3 solution (l:s = 10) twice at room temperature, for 2 h both times. The protonic form was then obtained by calcining the NH_4^+ form at 823 K for 5 h.

2.2. Characterization

The XRD patterns were recorded using a Rigaku Dmax/2500 X-ray diffractometer, which employed Ni-filtered Cu Kα radiation and was operated at 40 kV and 80 mA. A working plot can be obtained by plotting the intensity of the diffraction peak at $2\theta = 6.16$ versus the mass fraction of Y zeolite by measuring a series of physical mixtures with known mass fractions of Y zeolite. The mass fraction of Y zeolite in the BFZ composite can be estimated from the intensity of the XRD diffraction peak at $2\theta = 6.16$, which is the characteristic peak of Y zeolite.

The crystal size and morphology of the as-synthesized samples were investigated on a JSM-6301F scanning electron microscopy; the crystal faces and interface structure (crushed by 3 MPa pressure prior to the TEM analyses) were studied on a JEOL JEM-1011 transmission electron microscopy (TEM).

The N_2 adsorption at 77 K was performed in a NOVA 1200e gas sorption analyzer to study the micro- and mesoporosity of the zeolite crystals. The mesopore size distribution was calculated using the Barret–Joyner–Halenda (BJH) pore size model, as applied to the desorption branch of the isotherm [33]. The microporous structure was obtained from the *t*-plot analysis of the adsorption branch of the isotherm.

To measure pyridine adsorption, infrared spectra were obtained on a SHIMADZU FTIR-8400 spectrometer. To make a sample, ~12 mg of sample was pressed into a self-supporting wafer that was 10 mm in diameter. The wafer was first evacuated in situ in an IR cell at 573 K for 2 h, and the IR spectra were recorded at room temperature. Pyridine was then introduced into the cell at room temperature until the saturated adsorption was reached. Finally, the desorption of pyridine was performed at 423 K at 3×10^{-3} Pa of pressure, and the spectra were recorded at various temperatures.

All of the catalytic experiments were conducted at atmospheric pressure in a fixed-bed micro-reactor apparatus with a quartz tube (i.d. of 6 mm). Prior to each experiment, the H-zeolite was pressed into a cylinder, broken into 20–40 mesh particles, activated under flowing N_2 (50 mL/min) at 823 K for 2 h and then kept at the desired reaction temperature. Isopropylbenzene cracking was carried out at 523 K over 200 mg of catalyst; the molar ratio of isopropylbenzene to N_2 was kept constant at 0.014. The total gas flow at the

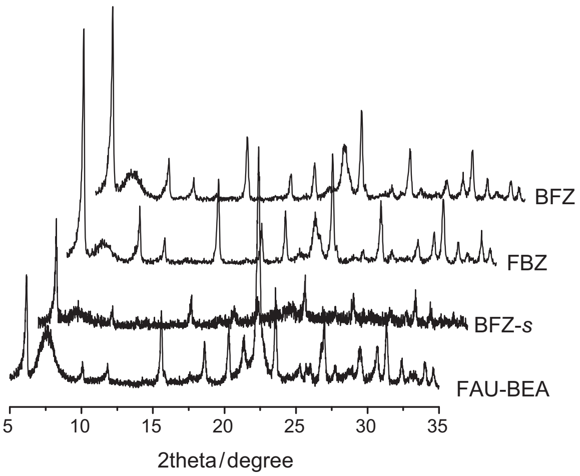

Fig. 1. XRD patterns of the as-synthesized zeolite composite samples.

reactor inlet was kept constant at 50 mL/min, and the lines were kept at 433 K using heating tapes. The methanol conversion was investigated with a WHSV of 2.26 $g^{-1} h^{-1}$ and a methanol partial pressure of 11.4 KPa; nitrogen was used as a carrier gas. All of the products were analyzed by an online gas chromatograph (Agilent1790) with a flame ionization detector (FID) and GDX-101 column.

3. Results and discussion

3.1. Synthesis and characterization

The powder XRD patterns of the four as-synthesized samples are presented in Fig. 1. The peaks at 6.08°, 15.72°, 18.75°, 20.43° and 23.67° are the characteristic diffraction peaks of Y zeolite phase, and the peaks at 7.63° and 22.19° are the β-zeolite characteristic peaks. These results indicate the co-existence of Y and β zeolite phases in the as-synthesized samples. Fig. 1 also shows that the sample BFZ-*s* has a relatively low crystallinity due to the massive amorphous bonder in the cylindrical-shaped extrudates.

The dissolution of the preformed β crystals in basic medium is a key procedure in obtaining BFZ and BFZ-*s* zeolite composites. The low stability of the β framework in alkaline solutions [12] can provide nutrients for the growth of Y zeolite during the second step of the synthesis. The action of the base is to promote the extraction of silicon species from the framework of the β zeolite. The extracted silicon species react with the aluminum species supplemented during the second step of the synthesis, which promotes the growth of Y zeolite. The experimental results show that the concentration of OH^- in the solution for synthesizing pure phase Y zeolite is approximately 0.9–1.0 mol/L, which is much lower than the 1.3–1.8 mol/L concentrations used for synthesizing the Y zeolite phase in the composite zeolite BFZ. On one hand, base plays an important role in the formation of the composite zeolites, but on the other hand, the formation of the Y zeolite phase in the composite zeolites differs from the synthesis of the pure phase Y zeolite. Excessive OH^- satisfies the requirement for a soluble silicon species for the growth of the Y zeolite phase in the composites by partly degrading the β zeolite crystals. The experimental results also show that the extracted silicon must match the supplemented aluminum species. An increased aluminum species supplemented at the second step of the synthesis need a relatively higher concentration of OH^- in the solution because the extraction of the silicon species is controlled by the alkalinity in the synthesis solution.

The formation process of the zeolite composite was also tracked by FT-IR spectroscopy, as shown in Fig. 2. The bands at 440–463 cm^{-1} are assigned to the O–T (Si or Al) bending vibrations, the bands at 520–580 cm^{-1} are assigned to the double ring external linkage vibrations [34,35], the bands at 740–760 cm^{-1} are assigned to the external linkage symmetrical stretching vibrations, and the bands around 1002 cm^{-1} are assigned to the internal tetrahedral asymmetrical stretching vibration. For BFZ and BFZ-*s*, the gradual transformation of β zeolite into an FAU structure was demonstrated by the simultaneous increase of the characteristic Y bands at 463 and 1002 cm^{-1} and a decrease of the β zeolite bands at 1071 and 1227 cm^{-1} during the formation of the composite zeolites. This indicates that the framework of the β zeolite was partially converted into Y zeolite; however, the gradual transformation of the FAU zeolite into the β zeolite structure was also proven by the simultaneous increase of the characteristic β zeolite bands at 1071 and 1227 cm^{-1} and decrease of FAU zeolite bands at 463 and 1002 cm^{-1} during the formation of the FBZ and FAU-BEA composite zeolites (not shown here). It is interesting that a new vibration band appears in the FBZ composites and shifts from 1035 cm^{-1} to 1050 cm^{-1} as the proportion of the β phase in the composites increases, which suggests a new internal tetrahedral asymmetrical stretching vibration at the interface between the Y zeolite and β zeolite in the composites [31]. The vibration band lies between 1002 cm^{-1} and 1071 cm^{-1}, which are the peak locations used to identify the Si/Al ratio of the framework of Y and β zeolites, respectively. The existence of the band in this region indicates that the Si/Al ratio of the composites is higher than that of Y zeolite but lower than that of β zeolite [31,36].

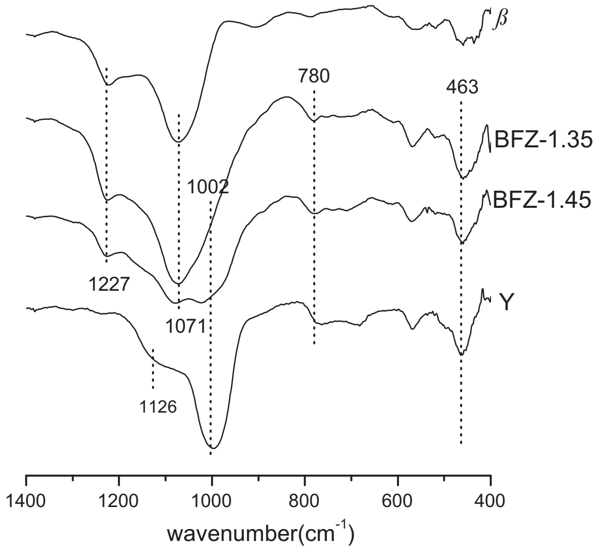

Fig. 2. FT-IR spectra of the as-synthesized composites and the reference Y and β zeolites.

The crystal morphology of the as-synthesized zeolite composites differs from those of Y or β zeolites, as shown in Fig. 3. The β zeolite and Y zeolite shows sphere-like crystal particles and an octahedral morphology, respectively (Fig. 3A). The sizes of the pure zeolite Y and pure zeolite β particles are ~1 μm, which is smaller than those of the composite (~2 μm). The relatively larger crystal size of the BFZ composite can be ascribed to the fact that Y zeolite crystals were grown around β zeolite particles. The morphology of the BFZ composite appears like rough spheres inlayed by many faujasite crystals (Fig. 3B). As shown in Fig. 3C, the crystal morphology of the FBZ zeolite composite still keeps the octahedral shape of the core Y zeolite despite having been covered by a polycrystalline shell composed of nano-sized β zeolite crystals. The SEM analysis of the as-synthesized FAU-BEA samples reveals that the composite is composed of FAU zeolite as the core and nanometer-sized

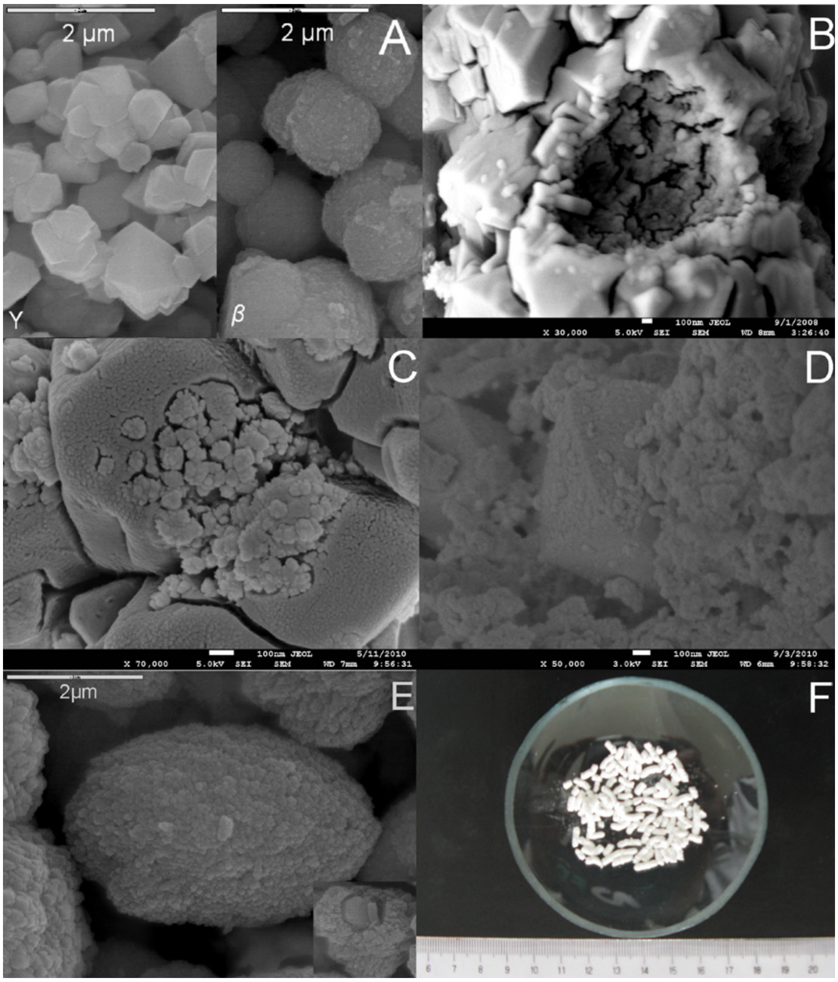

Fig. 3. SEM images (A–E) of zeolite composite samples and a photograph (F) of the precursory extrudates used for BFZ-s. (A) zeolites Y and β; (B) BFZ; (C) FBZ; (D) BFZ-*s*; (E) FAU-BEA (see Ref. [32]).

β zeolite as the polycrystalline shell (Fig. 3E). Fig. 3E also shows that the core-shell zeolite-zeolite FAU-BEA composite has lost the octahedral crystal morphology of the core (FAU) zeolite due to a relatively thicker shell compared with FBZ. It can be seen from Fig. 1 and Table 1 that there is a higher concentration ratio of β zeolite to Y zeolite in the FAU-BEA composite than that in FBZ. It can be seen from Fig. 3 that all of the zeolite crystals in polycrystalline shells have a smaller size than the crystals grown in the bulk, which could be caused by the steric hindrance provoked by the concurrently growing crystals in the shell [37]. Fig. 3D and F are the SEM images of BFZ-*s* and the photograph of the precursory extrudates, respectively. The FAU zeolite crystal with a typical octahedral crystal morphology can be clearly observed in the cross section of the cylindrical products. Interestingly, most of the particles are found to have enriched macroporosity in the SEM images, which should be attributed to the digestion of silica-alumina species or binder, especially the inner β zeolite, during the crystallization process. The β zeolite crystals are prone to being dissolved by the synthesis solution due to their instability in aqueous alkali solution with higher OH^- concentrations, and they therefore act as nutrients for the growth of Y zeolite during the hydrothermal process.

The adsorption–desorption of nitrogen on the purely microporous Y and β zeolites is a *type*-I isotherm, as shown in Fig. 4a, indicating the presence of micropores only. However, larger hysteresis loops occur in the adsorption–desorption isotherms of the zeolite composites, indicating the presence of the mesopores in the as-synthesized composite samples. The mesopores created in the composites can be caused by polycrystalline accumulation [32,37] as well as silicon extraction by the base in the synthesis solution [6,7,23]. Some N_2 adsorption–desorption data are presented in Table 1. It can also be inferred from Table 1 that the value of V_{meso} (volume of mesopore) in the composites follows an order of BFZ > FAU-BEA > FBZ > BFZ-*s*. The V_{meso} of the composites may be dependent on which of the polycrystalline accumulations and the silicon extractions dominates during the synthesis process. The BFZ zeolite composite has a larger V_{meso}, which increases with the increased alkalinity during the second step of the synthesis, indicating that the mesopores of the BFZ zeolite composite were mainly caused by the alkali-leaching action because of a higher alkalinity during the second step of the synthesis. The loss of silica by base treatment induces a significant change in the pore structure of the zeolite [6,7], and the alkaline-assisted hydrolysis of the Si–O–Si bonds from the zeolite framework was directed toward mesoporosity development [2,23]. Both FBZ and FAU-BEA are composites with a Y zeolite as the core and nano-sized β zeolites as the polycrystalline shell. A relatively low concentration of OH^- (about 0.4–0.5 mol/L) was present in the solution during the second step of the synthesis, resulting in a low amount of mesopores due to alkali-leaching. Therefore, the mesopores created in BFZ and FAU-BEA may mainly result from the polycrystalline accumulation rather than the alkali-leaching action. It is surprising that a lower value of V_{meso} was found in BFZ-*s*. This may be due to extensive silicon extraction from β zeolite, resulting in the formation of larger meso- or macropores, as shown in Fig. 3D. Table 1 also shows that the value

Table 1
Physico-chemical properties of the catalysts.

Samples	Y wt% content[a]	Si/Al ratio	S_{BET} (m^2/g)	S_{micro} (m^2/g)	S_{meso} (m^2/g)	V_{micro} (cm^3/g)	V_{meso} (cm^3/g)	Acidity (Py)[b] (mmol/g)		L/B (Py)	Conversion[c] (wt%)	HF[d]
								Lewis	Brönsted			
BFZ-1.30	15	8.1	486	364	80	0.19	0.21	0.58	0.49	1.2	77.2	0.078
BFZ-1.35	32	6.9	432	300	112	0.15	0.22	0.86	0.45	1.9	89.7	0.107
BFZ-1.40	47	6.1	454	355	130	0.18	0.22	1.05	0.46	2.3	91.3	0.129
BFZ-1.45	61	4.8	520	367	172	0.19	0.24	1.23	0.41	3.0	97.2	0.146
BFZ-1.50	75	3.9	514	378	130	0.19	0.27	1.30	0.37	3.5	88.1	0.100
BFZ-*s*	69	3.5	495	461	45	0.25	0.08	0.98	0.11	8.9	17.4	0.073
FAU-BEA	43	10.6	530	440	64	0.19	0.13	0.57	0.40	1.4	71.1	0.071
FBZ	71	5.7	578	491	72	0.23	0.11	0.69	0.43	1.6	82.1	0.084
BEA	–	12.5	517	367	29	0.18	0.04	0.24	0.58	0.4	84.7	0.045
FAU	–	2.5	738	701	9	0.36	0.02	1.16	0.53	2.2	53.6	0.012

[a] The relative content of the Y zeolite phase in the zeolite composite.
[b] Pyridine desorption was performed at 423 K.
[c] Catalytic cracking of isopropylbenzene at 523 K.
[d] The hierarchy factor (HF) is determined by the product (V_{micro}/V_{pore}) × (S_{meso}/S_{BET}) (see Ref. [30]).

of the BET surface area of the zeolite composites BFZ, BFZ-*s*, FBZ and FAU-BEA is lower than that of the corresponding physical mixture composed of pure microporous Y and β zeolites. The decrease in the BET surface area in the composites can be caused by the dissolution and partial amorphization of the original as-synthesized zeolite framework. The dissolution of the as-synthesized zeolite results in the breakdown of some of the micropores [3,15]. During the second step of the synthesis, the as-synthesized zeolite was etched by the synthesis solution, which leads to partial amorphization of its framework. Some channels may therefore be filled with debris from the amorphization of the framework and the silicon and/or aluminum scraps extracted from the framework. The decrease to the nanocrystalline range of the zeolite particles in the polycrystalline shell may also play a role in causing the deterioration of the ordering of the three-dimensional network [15].

As shown in Fig. 4b, the pore size distribution of the BFZ composite illustrates the existence of a mesopore structure with pore sizes ranging from 5 nm to 30 nm; the mesopore structures centered at 10 nm and 45 nm are found in the FAU-BEA and FBZ, respectively. The BFZ-*s* has a much wider pore distribution. However, the BJH pore size distribution derived from the desorption branch of the isotherm does not show a similar distribution in the pure micropore Y or β zeolites. It is important to note that the pronounced peak at 4 nm in the BJH desorption pore size distribution does not suggest a real pore but is instead due to the tensile strength effect (TSE) of the adsorbed phase [11,33,38,39].

Direct evidence for the presence of mesopores with a fairly uniform diameter of 5–30 nm is also provided by the TEM images of BFZ zeolite composites, as shown in Fig. 5A, which is in excellent agreement with N_2-adsorption analyses. This reveals the intracrystalline nature of the newly created mesopores as well as their distribution and size uniformity. The FBZ zeolite composite crystal displays a solid image (Fig. 5B) that is in good agreement with one of our recent studies [31]. It is surprising that almost no alteration is seen upon treatment in the FBZ zeolite composite crystal; no mesopores created in the core zeolite Y can be ascribed to the lower alkalinity during the second step of the synthesis, despite the higher reaction temperature. This further confirms that the new mesoporous structure observed in the adsorption–desorption of nitrogen on the FBZ zeolite composite is caused by the accumulation of nano-sized β zeolites in the polycrystalline shell, as observed by SEM (Fig. 3C). This result also indicates that relatively mild synthesis conditions (a lower alkalinity in the synthesis solution) hardly alter the core zeolite Y (FBZ and FAU-BEA).

The acidic properties of the as-synthesized zeolite composites were investigated by pyridine absorption, as measured by IR spectra (Fig. 6). All of the samples exhibit weak Lewis bond pyridine bands at ~1445 cm^{-1}, bands at 1454 cm^{-1} that correspond to a strong Lewis bond, and Brönsted bond pyridine bands at 1545 cm^{-1}, as well as the bands at 1490 cm^{-1} that are pyridine bands associated with both Brönsted- and Lewis-acid sites.

The Lewis/Brönsted ratios of the samples are obtained by calculating the peak area corresponding to the Lewis-acid sites and the Brönsted-acid sites in the IR spectra of pyridine adsorption of the as-synthesized samples; the results are shown in Table 1. Most of Lewis/Brönsted ratios are between those of the pure phase H-Y and H-β zeolites. However, BFZ-1.45 and BFZ-1.50 show higher Lewis/Brönsted ratios than that of the pure phase Y zeolite, indicating that the acidic properties in the zeolite composite are not a simple superposition of Y and β zeolites. The relatively high Lewis/Brönsted ratio in the composite could be caused by a number of reasons, including the destruction of some Si–O–Si and Si–O–Al bonds in the β zeolite and the formation of additional AlOH groups as well as the influence of the smaller crystal sizes of Y zeolites in the composites. The crystal size of the Y phase in the polycrystalline aggregate is much smaller than that of the pure Y zeolite. A smaller

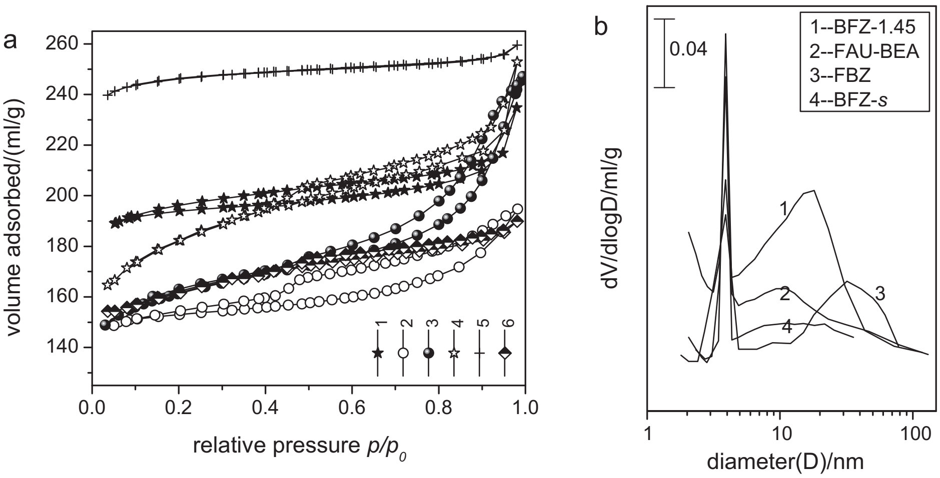

Fig. 4. (a) N_2 adsorption–desorption isotherms of the samples. (1) FBZ; (2) BFZ-*s*; (3) BFZ-1.45; (4) FAU-BEA; (5) Y; (6) β. (b) The corresponding BJH pore size distribution curves.

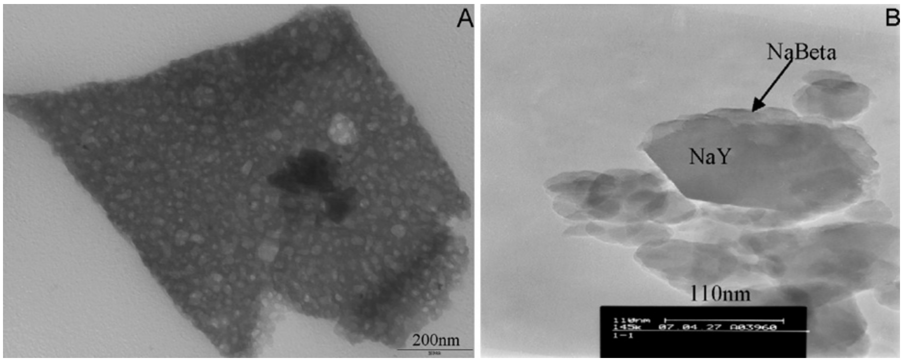

Fig. 5. High resolution TEM images. (A) BFZ and (B) FBZ (see Ref. [31]).

crystal size reduces the protonic acidity and increases the Lewis acidity [40,41]. The amorphization of the original zeolite framework and the aluminum scraps extracted from the framework may also play a role in enhancing the Lewis/Brönsted ratio.

Fig. 6 and Table 1 also show that the second crystallization in mild conditions (such as BFZ-1.35) hardly altered the amount of Brönsted-acid sites but led to a slight increase in the amount of Lewis-acid sites. It can also be inferred from Fig. 6 that the increased OH^- concentration during the second step of the synthesis increases Lewis-acid-site peak strength in the BFZ zeolite composite, although it slightly decreases Brönsted-acid-site the peak strength, which results in an increased Lewis/Brönsted ratio (Table 1). The enhanced OH^- concentration in the synthesis solution during the second step of the synthesis leads to the extra destruction of some Si–O–Si and Si–O–Al bonds in the β zeolite and the formation of additional AlOH groups during the composite synthesis. Not only the Brönsted-acid sites decrease with an increased damage of framework caused by the increasing alkalinity, also Lewis-acid sites increase with an increase in no-framework aluminum species as well as the partial amorphization of the framework caused by the increasing alkalinity. Despite an increasing Lewis/Brönsted ratio with the increasing alkalinity in the second step of the synthesis, the BFZ-*x* zeolite composites maintain relatively constant acidity values of the Brönsted-acid sites; the absolute acidity value of the Brönsted-acid sites was only slightly decreased from 0.49 mmol/g in BFZ-1.30 to 0.41 mmol/g in BFZ-1.45. The relatively stable absolute acidity values of the Brönsted-acid sites can be ascribed to the growth of Y zeolite in the polycrystalline shell, which partly eliminates the disadvantageous influence of the framework breakdown of the β zeolite crystals. The Y zeolite phase is increased from 15 wt% in BFZ-1.30 to 61 wt% in BFZ-1.45. These results also indicate that the alkalinity during the second step of the synthesis plays a very important role in the acidic properties and the distribution of these sites in the BFZ-*x* zeolite composite. These results also suggest that the Lewis/Brönsted ratio in the composite can be adjusted by controlling the alkalinity during the second step of the synthesis.

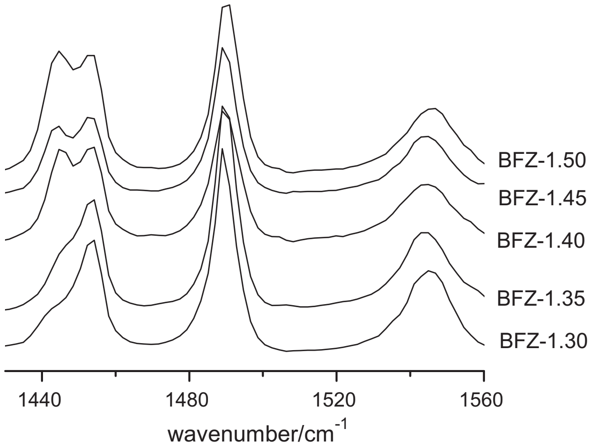

Fig. 6. IR spectra of pyridine adsorption of the BFZ-*x* zeolite composite (*x* stands for the concentration of OH^- (mol/L) during the second step of the synthesis).

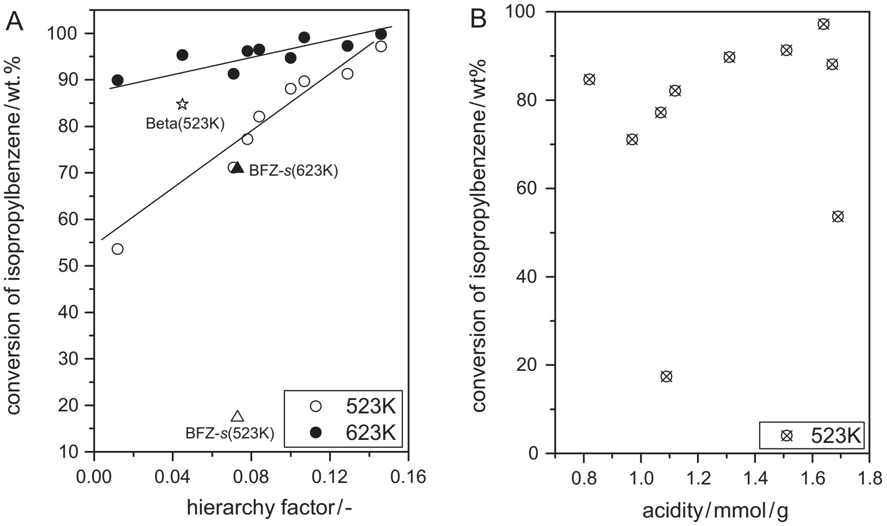

Fig. 7. Catalytic cracking of isopropylbenzene over the composite catalysts. (A) The relationship between the cracking activity and the HF (hierarchy factor) of the different catalysts. ☆ stands for the relationship between the cracking activity and the HF of β at 523 K; △ and ▲ are the relationships between the cracking activity and the HF of BFZ-*s* at 523 K and 623 K, respectively and (B) the relationship between the cracking activity and the acidity of different catalysts.

3.2. *Effects of hierarchical pores and tunable acidity*

The effects of hierarchical pores on the performance of the as-synthesized zeolite composites were investigated by measuring the catalytic cracking of isopropylbenzene. The relationship between the catalytic activity in the cracking of isopropylbenzene and the hierarchy factor of the different samples (purely microporous and hierarchical) has been plotted and is shown in Fig. 7A. The catalytic activities of most of the catalysts show a linear dependence with the hierarchy factor (except for β and BFZ-*s*). The catalytic cracking over the hierarchical zeolite composite is better than that of the purely microporous Y zeolite. The benefit of improved transport in the composite catalysts is therefore more influential than the loss of microporosity, and the net effect still results in an improved catalytic performance [30]. The relationship between the catalytic activity and the HF of the β and BFZ-*s* catalysts, which are shown in Fig. 7A, could be due to their different acidic properties. A lower activity is found for the BFZ-*s* catalyst, which can be ascribed to its smaller acidity (especially the much smaller number of Brönsted-acid sites (only 0.11 mmol/g), which is much lower than that of other catalysts) due to the presence of massive amorphous bonders; the higher activity of the β catalyst with a lower HF can be ascribed to its larger number of Brönsted-acid sites (as shown in Table 1). The slope of the line in Fig. 7A reflects the dependent degree of the activity of catalytic cracking of isopropylbenzene on the hierarchy factor. Fig. 7A also shows that with a relatively lower reaction temperature, such as 523 K, the cracking activity of isopropylbenzene strongly depends on the HF, indicating that the catalytic cracking of isopropylbenzene with the catalysts is a diffusion-controlled reaction at relatively low reaction temperatures; when the reaction temperature increases to 623 K, most of the catalytic activity still shows a linear dependence with the HF (except for BFZ-*s*), but the degree of the dependence is lower (it has a smaller linear lope). When isopropylbenzene cracking was performed at 523 K, the cracking activity shows a discrete dependence with the total acidity of different catalysts (Fig. 7B), indicating a diffusion-controlled reaction rather than the acidity-controlled reaction under a relatively low temperature. Fig. 7 also shows that the hierarchy factor put forward by Pérez-Ramírez et al. [30] is a very appropriate tool to classify hierarchically structured materials that have similar acidities and compositions (such as FAU-BEA, FBZ and BFZ, which were composed of FAU and BEA phase zeolites).

Methanol dehydration to DME was used in this study to evaluate the effect of tunable acidities on the hierarchically porous zeolite composites, and the composites are compared with the pure phase Y and β zeolite. It is well known that both the Brönsted-acid sites and Lewis-acid sites are responsible for the dehydration of methanol; the stronger Brönsted-acid sites are more responsible for the formation of hydrocarbons, but not for forming DME. Lewis-acid sites behave in the opposite manner: they tend to form DME, but not hydrocarbons. The Lewis/Brönsted ratios of different catalysts with different acidities were therefore used in this study to investigate their effect on the activity or selectivity in the dehydration of methanol. The experimental results show that the dehydration conversion of methanol over the zeolite composite is far higher than that over H-Y and somewhat lower than that over H-β. However, the selectivity of DME over the H-BFZ is much higher than that over H-β. The higher activity of H-β is attributed to its higher Brönsted-acid sites, as shown in Table 1. Despite the lower number of Brönsted-acid sites in BFZ-1.4 and BFZ-1.5 zeolite composites compared with a Y zeolite catalyst, much higher activity occurs with the two composite catalysts due to their unique crystalline structures. The dehydration of methanol is an exothermic reaction, and the mesopore structure created in the composite catalysts helps not only mass transfer but also heat transfer in the reaction [42]. In addition, the higher conversion of methanol on the H-BFZ zeolite composite could be caused by both the faster diffusion of products from the active centers in its channel and the higher accessibility of the Brönsted-acid sites resulting from the existence of the mesopores in the composite [5]. This accessibility partly eliminates the penalty of Brönsted-acid sites by introducing mesopores into the zeolite composites. The hierarchical pore system in the composite also gives the reactants easy access to the acid sites [22].

The relationship between the methanol dehydration activity as well as the selectivity of DME and the Lewis/Brönsted ratios of the different samples with different acidic properties has been plotted and is shown in Fig. 8A. It can be seen from Fig. 8 that the dehydration activity of methanol over the catalysts decreases linearly with an increasing Lewis/Brönsted ratio (Fig. 8A), while the selectivity of DME increases linearly with an increase in the

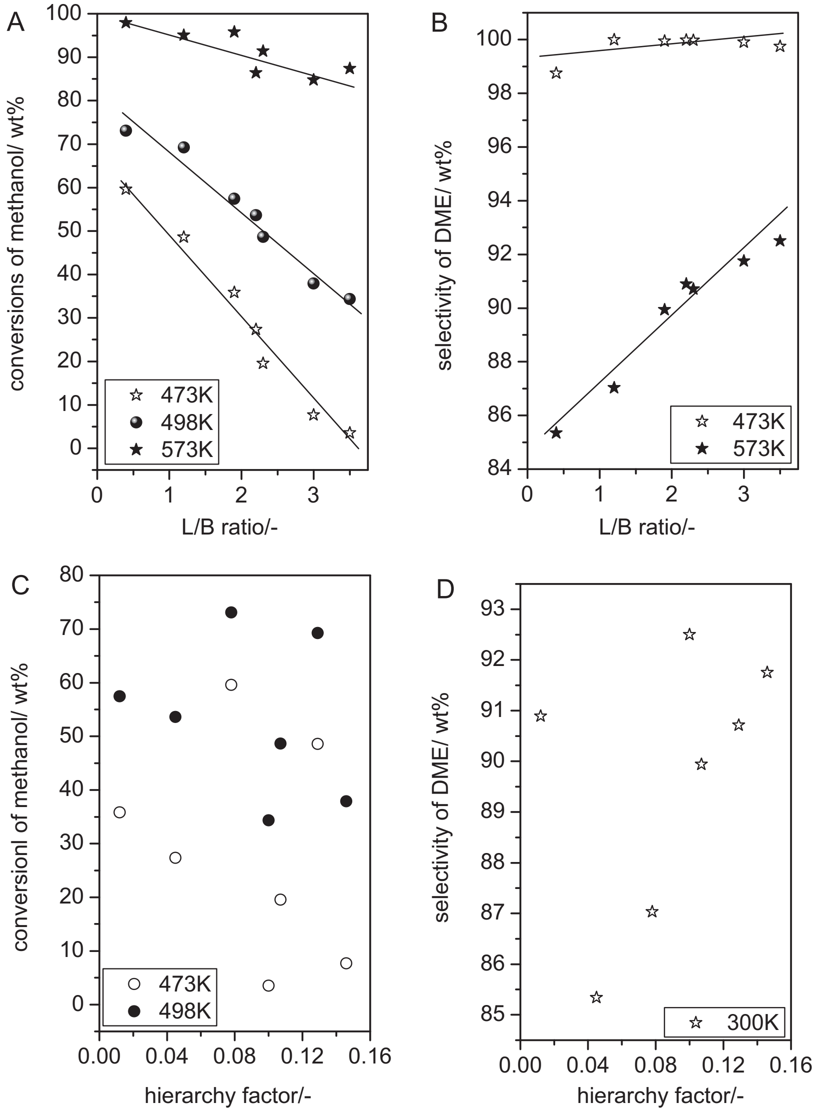

Fig. 8. Methanol dehydration to DME. (A) and (B) The dependent relationship of activity and selectivity on the Lewis/Brönsted ratio; (C) and (D) the relationship between the activity and the selectivity with the HF (hierarchy factor) of the different catalysts.

Lewis/Brönsted ratio (Fig. 8B). It can be inferred from Fig. 8 that a lower dehydration temperature results in a stronger dependence of the methanol dehydration activity on the Lewis/Brönsted ratio of the catalysts (Fig. 8A); however, for the selectivity of DME, a lower dehydration temperature results in a weaker dependence on the Lewis/Brönsted ratio (Fig. 8B). The relationship between the activity and the selectivity with the HF (hierarchy factor) of the different catalysts is shown in Fig. 8C and D, respectively. It can be seen that methanol dehydration over the composite catalysts shows a discrete relationship with the HF, showing a good linear dependence with the Lewis/Brönsted ratio (Fig. 8A and B). This indicates that methanol dehydration is mainly controlled by the acidity of the catalyst.

Fig. 8B also shows that an increased reaction temperature leads to a decreased selectivity for DME. It is well known that methanol conversion can proceed on molecular sieves either as a simple dehydration, yielding DME and water as the only products, or as a process of deep dehydration, producing hydrocarbons [43]. Therefore, the increased reaction temperature is responsible for the formation of hydrocarbons but not for forming DME due to the stronger Brönsted-acid sites, as both weak and strong acid sites facilitate the simple dehydration reaction, but only strong acid sites facilitate the deep dehydration and the consequent formation of hydrocarbons [44]. When the temperature arrived at 573 K, a large amount of byproducts was observed in H-β, and the catalyst was coked. This indicates that the strong surface acidity (especially the strong Brönsted-acid sites) in the catalysts converts methanol and DME to hydrocarbons and causes coking [44]. The higher DME selectivity of the composite catalysts can be ascribed to its higher Lewis/Brönsted ratio. In addition, the hierarchical pore structure in the composite catalysts may also lead to a decreased residence time of DME in the channels such that fewer secondary reactions occur.

Fig. 9 displays the durability of the H-BFZ-1.45 catalyst for methanol dehydration at 548 K. The sample exhibits a slight deactivation over 72 h. Published data [44] indicated that deactivation in the methanol dehydration reaction was caused by the deep dehydration of methanol and DME on strong Brönsted-acid sites inside the pores of zeolites. However, a 72 wt% conversion of methanol can still be found in the catalyst. Fig. 9 also shows that the catalyst maintains a 100 wt% selectivity of DME despite the deactivation.

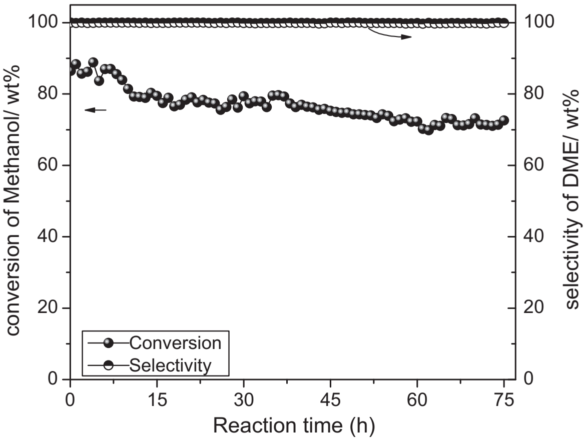

Fig. 9. Durability of methanol dehydration over H-BFZ-1.45 at 548 K.

4. Conclusions

Four zeolite composites with different acidities and pore structures were prepared. The Lewis/Brönsted ratio in the as-synthesized composite can be adjusted by controlling the synthesis conditions. The effects of hierarchical pores on the performances of the as-synthesized zeolite composite samples were tested for the catalytic cracking of isopropylbenzene, and the influence of the tunable acidity in the as-synthesized BFZ zeolite composite was investigated using the dehydration of methanol to DME. The catalytic activity of isopropylbenzene cracking strongly depends on the hierarchy factor, indicating that isopropylbenzene cracking over the catalysts is a diffusion-controlled reaction at a relatively low reaction temperature. The dehydration of methanol to DME shows that both the DME selectivity and the methanol conversion have a good linear dependence with the Lewis/Brönsted ratio; the dehydration activity of methanol over the catalysts decreases linearly with an increase in the Lewis/Brönsted ratio, while the selectivity of DME increases linearly with an increased Lewis/Brönsted ratio. A conclusion can be drawn that the hierarchy factor is an appropriate tool to classify hierarchically structured materials with similar acidities and compositions in a diffusion-controlled reaction (such as isopropylbenzene cracking); however, for the acidity-controlled reactions (such as methanol dehydration to DME), the hierarchy factor may only play a negligible role.

Acknowledgements

This work is supported by the “973” project (No. 2005CB221204) and SinoPEC (No. 107009).

References

[1] S. van Donk, A. Broersma, O.L.J. Gijzeman, J.A. van Bokhoven, J.H. Bitter, K.P. de Jong, J. Catal. 204 (2001) 272.
[2] J. Pérez-Ramírez, C.H. Christensen, K. Egeblad, C.H. Christensend, J.C. Groen, Chem. Soc. Rev. 37 (2008) 2530.
[3] Y. Tao, H. Kanoh, L. Abrams, K. Kaneko, Chem. Rev. 106 (2006) 896.
[4] S. van Donk, A.H. Janssen, J.H. Bitter, K.P. de Jong, Catal. Rev. Sci. Eng. 45 (2003) 297.
[5] J. Zheng, X. Zhang, Y. Zhang, J. Ma, R. Li, Micropor. Mesopor. Mater. 122 (2009) 264.
[6] J.C. Groen, T. Bach, U. Ziese, A.M.P. van Donk, K.P. de Jong, J.A. Moulijn, J. Pérez-Ramírez, J. Am. Chem. Soc. 127 (2005) 10792.
[7] J.C. Groen, W. Zhu, S. Brouwer, S.J. Huynink, F. Kapteijn, J.A. Moulijn, J. Pérez-Ramírez, J. Am. Chem. Soc. 129 (2007) 355.
[8] J.C. Groen, L.A.A. Peffer, J.A. Moulijn, J. Pérez-Ramírez, Colloid Surf. A 241 (2004) 53.
[9] J.C. Groen, J.A. Moulijn, J. Pérez-Ramírez, Micropor. Mesopor. Mater. 87 (2005) 153.
[10] J.C. Groen, A. Brückner, E. Berrier, L. Maldonado, J.A. Moulijn, J. Pérez-Ramírez, J. Catal. 243 (2006) 212.
[11] J.C. Groen, L.A.A. Peffer, J.A. Moulijn, J. Pérez-Ramírez, Chem. Eur. J. 11 (2005) 4983.
[12] J.C. Groen, S. Abelló, L.A. Villaescusa, J. Pérez-Ramírez, Micropor. Mesopor. Mater. 114 (2008) 93.
[13] J.C. Groen, J.C. Jansen, J.A. Moulijn, J. Pérez-Ramírez, J. Phys. Chem. B 108 (2004) 13062.
[14] M. Hartmann, Angew. Chem. Int. Ed. 43 (2004) 5880.
[15] Y. Tao, H. Kanoh, K. Kaneko, Langmuir 21 (2005) 504.
[16] H. Wang, T. Pinnavaia, J. Angew. Chem. Int. Ed. 45 (2006) 7603.
[17] D.P. Serrano, J. Aguado, J.M. Escola, J.M. Rodríguez, A. Peral, Chem. Mater. 18 (2006) 2462.
[18] Z. Yang, Y. Xia, R. Mokaya, Adv. Mater. 16 (2004) 727.
[19] M. Tromp, J.A. van Bokhoven, M.T. Garriga Oostenbrink, J.H. Bitter, K.P. de Jong, D.C. Koningsberger, J. Catal. 190 (2000) 209.
[20] J. Zheng, Q. Zeng, J. Ma, X. Zhang, W. Sun, R. Li, Chem. Lett. 39 (2010) 330.
[21] V.V. Ordomsky, V.Y. Murzin, Y.V. Monakhova, Y.V. Zubavichus, E.E. Knyazeva, N.S. Nesterenko, I.I. Ivanova, Micropor. Mesopor. Mater. 105 (2007) 101.
[22] N.S. Nesterenko, F. Thibault-Starzyk, V. Montouillout, V.V. Yuschenko, C. Fernandez, J.-P. Gilson, F. Fajula, I.I. Ivanova, Micropor. Mesopor. Mater. 71 (2004) 157.
[23] J.S. Jung, J.W. Park, G. Seo, Appl. Catal. A: Gen. 288 (2005) 149.
[24] K. Egeblad, C.H. Christensen, M. Kustova, C.H. Christensen, Chem. Mater. 20 (2008) 946.
[25] C.J.H. Jacobsen, C. Madsen, J. Houzvicka, I. Schmidt, A. Carlsson, J. Am. Chem. Soc. 122 (2000) 7116.
[26] I. Schmidt, A. Boisen, E. Gustavsson, K. Ståhl, S. Pehrson, S. Dahl, A. Carlsson, C.J.H. Jacobsen, Chem. Mater. 13 (2001) 4416.
[27] Y. Tao, H. Kanoh, K. Kaneko, J. Am. Chem. Soc. 125 (2003) 6044.
[28] Y. Tao, Y. Hattori, A. Matumoto, H. Kanoh, K. Kaneko, J. Phys. Chem. B 109 (2005) 194.
[29] Y. Tao, H. Kanoh, K. Kaneko, J. Phys. Chem. B 107 (2003) 10974.
[30] J. Pérez-Ramírez, D. Verboekend, A. Bonilla, S. Abelló, Adv. Funct. Mater. 19 (2009) 3972.
[31] X. Zhang, Q. Guo, B. Qin, Z. Zhang, F. Ling, W. Sun, R. Li, Catal. Today 149 (2010) 212.
[32] J. Zheng, X. Zhang, Y. Wang, Y. Bai, W. Sun, R. Li, J. Porous Mater. 16 (2009) 731.
[33] H. Zhu, Z. Liu, Y. Wang, D. Kong, X. Yuan, Z. Xie, Chem. Mater. 20 (2008) 1134.
[34] G.W. Skeels, D.W. Breck, in: D.H. Olson, A. Bisio (Eds.), Proceedings of 6th International Zeolite Conference, Butterworths, Guildford, 1984.
[35] B.A. Holmberg, H.T. Wang, J.M. Norbeck, Y. Yan, Micropor. Mesopor. Mater. 59 (2003) 13.
[36] B.A. Holmberg, H.T. Wang, Y.S. Yan, Micropor. Mesopor. Mater. 74 (2004) 189.
[37] Y. Bouizi, L. Rouleau, V.P. Valtchev, Chem. Mater. 18 (2006) 4959.
[38] J.C. Groen, L.A.A. Peffer, J. Pérez-Ramírez, Micropor. Mesopor. Mater. 60 (2003) 1.
[39] J.C. Groen, J. Pérez-Ramírez, Appl. Catal. A: Gen. 268 (2004) 121.
[40] A. Simon-Masseron, J.P. Marques, J.M. Lopes, F. Ramôa Ribeiro, I. Gener, M. Guisnet, Appl. Catal. A: Gen. 316 (2007) 75.
[41] A. Chica, A. Corma, J. Catal. 187 (1999) 167.
[42] R. Dimitrova, G. Gunduz, L. Dimitrov, T. Tsoncheva, S. Yialmaz, E.A. Urquieta-Gonzalez, J. Mol. Catal. A: Chem. 214 (2004) 265.
[43] D. Mao, W. Yang, J. Xia, B. Zhang, Q. Song, Q. Chen, J. Catal. 230 (2005) 140.
[44] D. Jin, B. Zhu, Z. Hou, J. Fei, H. Lou, X. Zheng, Fuel 86 (2007) 2707.